Journal of Biomedical Optics

BiomedicalOptics.SPIEDigitalLibrary.org

Multidistance diffuse correlation spectroscopy for simultaneous estimation of blood flow index and optical properties

Parisa Farzam
Turgut Durduran

SPIE.

Multidistance diffuse correlation spectroscopy for simultaneous estimation of blood flow index and optical properties

Parisa Farzam and Turgut Durduran*
ICFO–Institut de Ciències Fotòniques, Mediterranean Technology Park, 08860 Castelldefels, Barcelona, Spain

Abstract. Traditionally, diffuse correlation spectroscopy (DCS) measures microvascular blood flow by fitting a physical model to the measurement of the intensity autocorrelation function from a single source-detector pair. This analysis relies on the accurate knowledge of the optical properties, absorption, and reduced scattering coefficients of the medium. Therefore, DCS is often deployed together with diffuse optical spectroscopy. We present an algorithm that employs multidistance DCS (MD-DCS) for simultaneous measurement of blood flow index, as well as an estimate of the optical properties of the tissue. The algorithm has been validated through noise-free and noise-added simulated data and phantom measurements. A longitudinal *in vivo* measurement of a mouse tumor is also shown. MD-DCS is introduced as a stand-alone system for small source-detector separations (<2 cm) for noninvasive measurement of microvascular blood flow. [DOI: 10.1117/1.JBO.20.5.055001]

Keywords: near-infrared spectroscopy; diffuse correlation spectroscopy; blood flow; hemodynamics.

Paper 140623RR received Sep. 27, 2014; accepted for publication Mar. 31, 2015; published online May 4, 2015.

1 Introduction

Diffuse correlation spectroscopy (DCS) is a relatively new technique based on temporal speckle fluctuations of the diffuse light for blood flow measurements in the microvasculature.[1,2] DCS has been widely used in different medical applications such as neurology and oncology.[3–5] In traditional DCS analysis, the optical properties of the medium, absorption (μ_a), and reduced scattering (μ_s') coefficients should be known and the errors in the estimation of these parameters influence the calculated blood flow index (BFI). Most significant errors come from errors in estimating the scattering coefficient, whereas the results are less sensitive to the absorption coefficient.[6] DCS is often applied in tandem with a near-infrared diffuse optical spectroscopy (NIRS/DOS) system in order to get more physiological information and also because μ_a and μ_s' change in time.[2]

Previously, it has been shown that simultaneously fitting μ_s' and/or μ_a with BFI was impractical from a single intensity autocorrelation measurement, i.e., from a single source-detector pair,[7] due to strong coupling between the parameters. We have hypothesized and observed that the effect of this coupling is dependent on the source-detector separation which has led us to explore if there is a regime where multiple source-detector separations in an analogous fashion to continuous-wave or frequency-domain NIRS/DOS can be used to completely or partially decouple these parameters.

In this work, we describe a multidistance DCS (MD-DCS) algorithm for simultaneous measurement of μ_a, μ_s', and BFI in small source-detector separations using noise-added simulated data, phantom measurements, and on a longitudinal *in vivo* study of a mouse tumor.

*Address all correspondence to: Turgut Durduran, E-mail: turgut.durduran@icfo.es

2 Theory, Algorithms, and Experimental Methods

Information about the dynamics of the scatterers, in most cases about the motion of red blood cells, i.e., blood flow, can be derived from the measurement of the intensity autocorrelation of a single speckle generated by diffuse light in tissues.[2] For DCS analysis, we converted measured intensity autocorrelation g_2 to field autocorrelation function using the Siegert relation $g_1(\tau) = \{\sqrt{[g_2(\tau) - 1]/\beta}\}$, where β is a constant determined primarily by the collection optics of the experiment. We note that in our experiments, we use nonpolarized light sources and single-mode fibers without polarizers to collect the diffuse light. Therefore, in our experiments, $\beta \approx 0.5$.

The electric field autocorrelation function (G_1), Eq. (1), and the normalized field autocorrelation function (g_1) can then be derived and a correlation diffusion model can be used to fit the data and extract the blood flow information.[2] The Green's function solution of the correlation diffusion equation for semi-infinite boundary conditions is given by

$$G_1(\rho,\tau) = \frac{3\mu_s'}{4\pi}\left\{\frac{\exp[-K(\tau)r_1]}{r_1} - \frac{\exp[-K(\tau)r_b]}{r_b}\right\}. \quad (1)$$

Here, τ is the delay time, $r_1 = \sqrt{(1/\mu_s')^2 + \rho^2}$, $r_b = \sqrt{(2z_b + 1/\mu_s')^2 + (1/\mu_s')^2 + \rho^2}$, and $K(\tau) = \sqrt{3\mu_a\mu_s' + 6\mu_s'^2\kappa^2\alpha\tau\mathrm{BFI}}$. α is the fraction of photon scattering events that occur from moving particles in the medium and κ is the wave-number of light in the medium.

Here, we posit that the source-detector separation dependence of the g_1 allows us to decouple the contribution of static (μ_a and μ_s') and dynamic, BFI, properties of the medium under

1083-3668/2015/$25.00

certain conditions. Therefore, we fit for all desired variables (μ_a, μ_s', and BFI) using a single penalty function, χ^2, defined as

$$\chi^2 = \sum_{i=1}^{N_\rho}\sum_{j=1}^{N_\tau}[g_1^{\text{theory}}(\rho_i,\tau_j,\text{BFI},\mu_s',\mu_a) - g_1^{\text{measured}}(\rho_i,\tau_j,\text{BFI},\mu_s',\mu_a)]^2, \quad (2)$$

where ρ_i is the i'th source-detector separation and N_ρ is the number of source-detector separations. τ_j is the j'th delay time and N_τ is the number of delay times. In our implementation, the Nelder–Mead derivative-free simplex method ("fminsearch") implemented in MATLAB® (Mathworks) was used to minimize this function.

There is more information in the MD-DCS measurements since we are recording the average detected intensity in an analogous fashion to continuous-wave NIRS/DOS. This measured intensity at each detector position from the continuous-wave DCS laser can also be utilized to obtain the effective attenuation coefficient ($\mu_{\text{eff}} = \sqrt{3\mu_a\mu_s'}$) to improve the robustness of the algorithm by constraining the relationship between absorption and scattering. We will demonstrate the utility of these in experimental results.

There is one important caveat that we should mention here: DCS uses the intensity autocorrelation functions and, as such, it does not suffer from the so-called source-detector coupling problems. NIRS/DOS, on the other hand, uses the source-detector separation dependence of the intensity alone to measure μ_{eff} which requires that these coefficients are calibrated. For the purposes of this work, we did not construct a new probe and our existing probe configuration does not allow the measurement of μ_{eff} through the DCS fibers due to this calibration issue.[8,9] However, it contains a set of self-calibrating NIRS/DOS fibers that can be used for the measurement of μ_{eff} and we utilized them in some of the experimental data. It is beyond the scope of this paper to overcome this limitation.

2.1 *Numerical Data Generation*

We have simulated 125 media with five different absorption (μ_a from 0.04 to 0.16 with steps of 0.03 cm^{-1}), five different scattering (μ_s' from 4 to 16 with steps of 3 cm^{-1}), and five different flow (BFI from 4×10^{-9} to 16×10^{-9} with steps of 3×10^{-9} cm^2/s).

For the main results, the same source-detector separations (2.5 to 5.0 mm) as our existing probe, which is used for phantom and *in vivo* measurements,[8] were simulated. We have also simulated intermediate (10 to 20 mm) and large (20 to 34 mm) optode distances that are shown in Appendices A and B. In a single distance fitting for each separation category (small, intermediate, and large), one separation in the middle is chosen as a representative.

Realistic noise is added to the simulated autocorrelation curves using the previously published DCS noise model.[10] In a DCS experiment, the normalized field autocorrelation function decays exponentially [$g_1(\tau) = e^{-\Gamma\tau}$]. The optical/mechanical properties of medium and experimental conditions define the value of Γ. The standard deviation [$\sigma(\tau)$, noise] of the measured intensity autocorrelation, $g_2(\tau)$, at each delay time (τ) is estimated to be

$$\sigma(\tau) = \sqrt{T/t}\left[\beta^2\frac{(1+e^{-2\Gamma T})(1+e^{-2\Gamma\tau})+2m(1-e^{-2\Gamma T})e^{-2\Gamma\tau}}{1-e^{-2\Gamma T}}\right]^{\frac{1}{2}} + \sqrt{T/t}[2\langle n\rangle^{-1}\beta(1+e^{-2\Gamma\tau})+\langle n\rangle^{-2}(1+\beta e^{-\Gamma\tau})]^{\frac{1}{2}}. \quad (3)$$

Here, T is the correlator bin time interval, and m is the bin index corresponding to the delay time τ. In our correlator, the bin time interval is $T = 200$ ns for the first 16 channels and is doubled every eight channels afterward. t is the total averaging time which is assumed to be 1 min in the following simulations. The average number of photons within bin time T is $\langle n\rangle$, i.e., $\langle n\rangle = IT$, where I is the detected photon count rate. The maximum photon count rate of 1000 kHz is assigned to the smallest source-detector separations. This is the upper limit of the combination of the avalanche photodiodes and digital correlators that are used in the experimental setup. The photon count rate for each optode is calculated from Green's function solution for photon fluence in semi-infinite boundary conditions.[2]

Furthermore, we have simulated 16 acquisitions in each optode distance which could be experimentally acquired either by having multiple fibers for each detector[11,12] and/or by repeated measurements. We note that these simulations provide a usable signal-to-noise ratio even at the largest source-detector separations which is often not available for real-life DCS experiments. This was chosen to avoid the simulation results being dominated simply by signal-to-noise levels and a realistic phantom and *in vivo* data were utilized to validate the algorithms.

2.2 *Quantification of the Error of the Fitted Blood Flow Index*

To compare the efficacy of MD-DCS fitting with and without providing μ_{eff} in different separation types (small, intermediate, and large), we have calculated the error in fitted BFI (ε_{BFI}). For each of the simulated BFI, there are five different absorption (μ_a) and scattering (μ_s'). For each BFI, the estimation error is calculated as the root mean square of the relative difference between fitted and expected values of BFI as

$$\varepsilon_{\text{BFI}} = \sqrt{\frac{1}{N}\sum_{\mu_s'}\sum_{\mu_a}\left(\frac{\text{BFI}_{\text{fitted}}-\text{BFI}_{\text{expected}}}{\text{BFI}_{\text{expected}}}\right)^2}, \quad (4)$$

where N is the total number of different sets of μ_a and μ_s' for a given BFI (in this case: $5\times5 = 25$).

2.3 *Evaluation of the Penalty Function*

For a simulated DCS measurement with $\mu_a = 0.1$ cm^{-1}, $\mu_s' = 10$ cm^{-1}, and BFI $= 10^{-8}$ cm^2/s, we have evaluated the penalty function, χ^2, for discrete values of $0.09 \le \mu_a \le 0.11$ cm^{-1}, $9 \le \mu_s' \le 11$ cm^{-1}, and $0.9\times10^{-8} \le \text{BFI} \le 1.1\times10^{-8}$ cm^2/s. The χ^2 is calculated for two cases: multidistance DCS (MD-DCS) and single-distance DCS (SD-DCS) fitting. MD-DCS fits for eight source-detector separations (2.5 to 5.0 mm) and in SD-DCS, the fourth separation is chosen as a representative (3.6 mm).

2.4 *Tissue Simulating Liquid Phantoms*

As mentioned above, the systematic error due to the coupling of BFI with the optical properties is dependent strongly on μ_s' and relatively weakly on μ_a. To that end, MD-DCS was then validated on liquid phantoms where μ_s' was titrated and μ_a and BFI were kept constant. In these MD-DCS measurements, a handheld probe with eight source-detector separations from 2.5 to 5.0 mm (2.5, 2.9, 3.2, 3.6, 3.9, 4.3, 4.6, and 5.0 mm) is utilized based on our previous murine tumor measurements.[9] Eleven sets of data were acquired with an averaging time of 1 s per acquisition, and the probe was removed then replaced and this procedure was repeated 10 times. In other words, a total of 110 measurements were obtained for each source-detector position. This procedure mimics our *in vivo* measurement protocols.

Seven liquid phantoms starting with 160 ml of tap water with stepwise 5 ml increments (except 10 ml for the last step) of Lipofundin MCT 20% (BBRAUN, Spain) were measured. The results are shown with box-plots for each phantom representing the variability of each measurement. Prior to this study, μ_s' of 1% Lipofundin was measured by a time-resolved spectroscopy instrument and, assuming the linear relation between μ_s' and the Lipofundin concentration, the expected μ_s' for each phantom was calculated.

2.5 *In Vivo Measurements on a Mouse Tumor*

The data were acquired with a hybrid system using a broadband, multidistance NIRS/DOS device to measure the optical properties. The source and detector fibers for both NIRS/DOS and DCS systems were combined on a single handheld probe (six separations from 1.9 to 5.0 mm).[9] The fitted values of μ_a and μ_s' from the MD-DCS method are then compared with these NIRS/DOS results. The fitting of μ_a and μ_s' from broadband continuous-wave spectroscopy data was previously demonstrated.[9,13] This also allows us to compare the MD-DCS fitted BFI values with those obtained by single source-detector pair DCS measurements with NIRS/DOS input—presumably providing the best estimate of the bulk optical properties.

This mouse was part of a study where an antiangiogenic therapy was administered on an implanted renal cell carcinoma model.[9] The mouse was measured just before the start of therapy (day 0), received the therapy twice per week, and was measured before each drug injection. In every measurement, in order to have better statistics of the optical properties of tumor, we repositioned the probe 10 times and took 11 data points at each position with an averaging time of 1 s per acquisition. In total, 110 measurements were obtained for each source-detector position. The results are represented as means with error bars showing the standard deviation at each day of the measurement.

To compare whether the measured BFI by MD-DCS and hybrid device are in agreement, we have utilized a two-tailed student test (with 95% confidence interval). We did not repeat this analysis for other mice in the study since the biostatistical analysis of the therapy effects is beyond the scope of this paper.

3 Results

3.1 *Penalty Function in Single-Distance and Multidistance Diffuse Correlation Spectroscopy Fitting*

As described above, a simulated DCS measurement with $\mu_a = 0.1\ \text{cm}^{-1}$, $\mu_s' = 10\ \text{cm}^{-1}$, and $\text{BFI} = 10^{-8}\ \text{cm}^2/\text{s}$ was used to calculate the penalty function χ^2 defined in Eq. (2) for a range of values. The χ^2 for the expected μ_a plane, i.e., the plane where $\mu_a = 0.1\ \text{cm}^{-1}$, is shown in Fig. 1 for SD-DCS (a) and MD-DCS (b).

In the single distance fitting, the minimum of the penalty function occurs over a wide range of values of optical parameters and BFI as previously reported.[7] Adding more measurements from multiple source-detector separations, i.e., the MD-DCS approach, confines χ^2 to a smaller area which leads to better convergence of the algorithm.

3.2 *Multidistance and Single-Distance Diffuse Correlation Spectroscopy Fitting on the Simulated Data*

3.2.1 *Noise-free simulations*

We have applied SD-DCS and MD-DCS to noise-free data for eight source-detector separations from 2.5 to 5.0 mm (2.5, 2.9, 3.2, 3.6, 3.9, 4.3, 4.6, and 5.0 mm). Figure 2 shows that both SD-DCS and MD-DCS can accurately retrieve all parameters

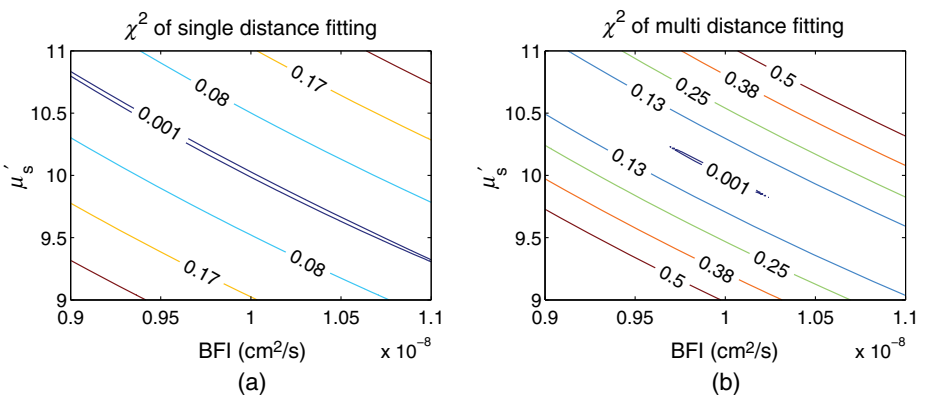

Fig. 1 The penalty function of (a) SD-DCS and (b) MD-DCS. χ^2 is plotted for the expected μ_a plane, i.e., the plane where $\mu_a = 0.1\ \text{cm}^{-1}$.

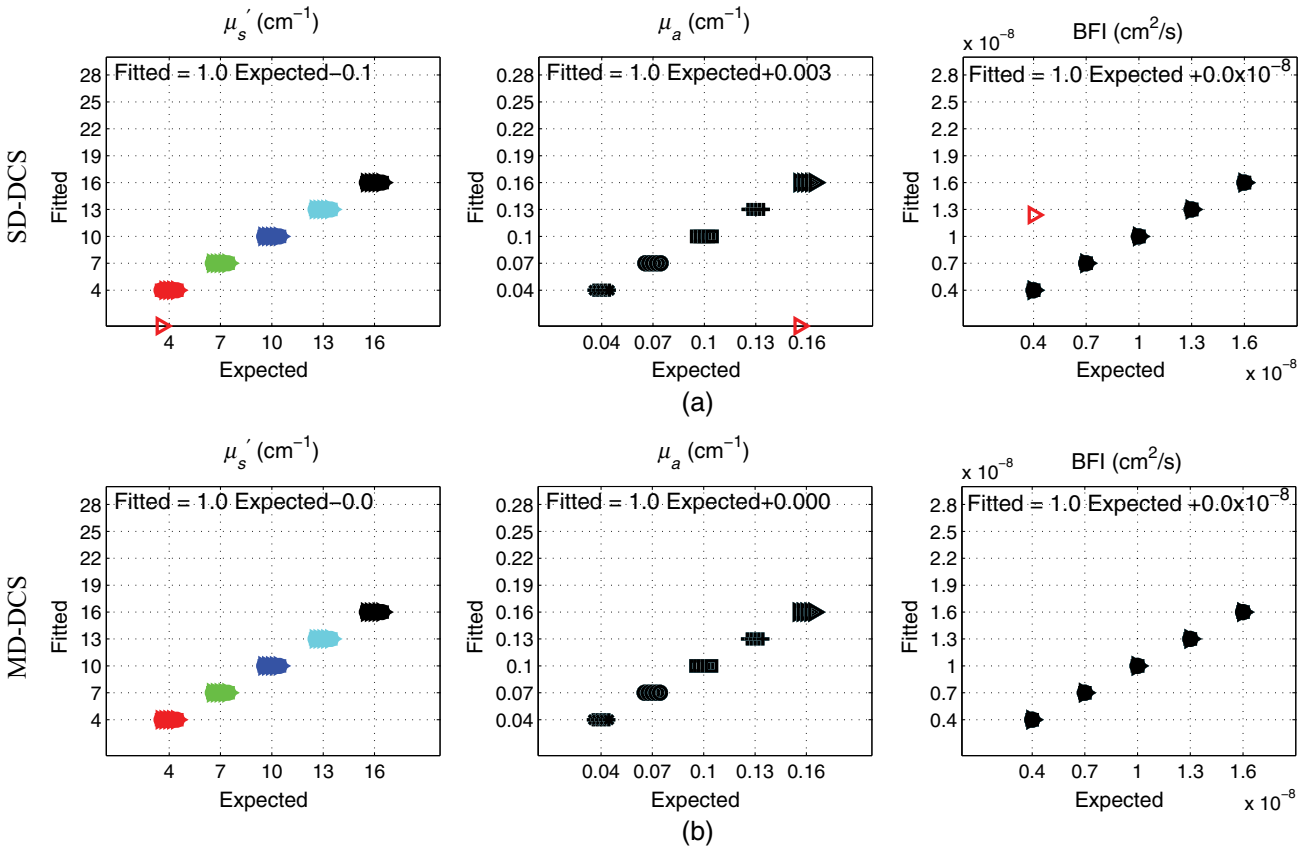

Fig. 2 The values of fitted μ_s', μ_a, and BFI versus the expected values in noise-free, small source-detector separations (2.5 to 5.0 mm). The top three plots are the results of SD-DCS and the bottom ones are from MD-DCS fitting. The slope (expected slope is 1) and intercept (expected intercept is 0) of the fitted values versus expected ones for each parameter are displayed in the inset. Each color represents one μ_s' (red: $\mu_s' = 4$, green: $\mu_s' = 7$, blue: $\mu_s' = 10$, cyan: $\mu_s' = 13$, and black: $\mu_s' = 16$) and each μ_a is shown by a different marker (star: $\mu_a = 0.04$, circle: $\mu_a = 0.07$, square: $\mu_a = 0.10$, cross: $\mu_a = 0.13$, and triangle: $\mu_a = 0.16$). Dodging is used (moving the points slightly across the *x*-axis) for better visualization of BFI values where for each μ_s' or μ_a, BFI increases from left to right. (a) SD-DCS and (b) MD-DCS retrieve all three parameters μ_s' (left), μ_a (middle), and BFI (right) accurately except for one point with the lowest μ_s'/BFI and highest μ_a that SD-DCS fails to fit.

except for one point with lowest μ_s'/BFI and highest μ_a that SD-DCS fails to fit. We have performed a similar fitting for intermediate (10 to 20 mm) and large (20 to 34 mm) separations, and the results are shown in Appendix A. While MD-DCS fits all the parameters (μ_a, μ_s', and BFI) without any error, SD-DCS has considerable error even in noise-free data and the error rises by increasing the source-detector separation (Figs. 7 and 8).

3.2.2 *Noise-added simulations*

We have applied SD-DCS and MD-DCS to noise-added simulated data in small optode distances (2.5 to 5 mm), and the results are presented in Fig. 3. It shows that SD-DCS has a considerable error when dealing with realistic experimental noise, whereas MD-DCS fits all parameters with a high accuracy (less than 5% error).

The results of fitting for intermediate and large separations are shown in Appendix B. In these simulations, it was observed that the accuracy of the fitted parameters by MD-DCS decreases when the source-detector separation is larger than ~2 cm. Therefore, from this point on, we focus on small source-detector separations for both phantom and *in vivo* validations.

3.3 *Multidistance Diffuse Correlation Spectroscopy Fitting on the Liquid Phantom Data*

As explained above, to validate the algorithm in experimental conditions, we have measured homogenous liquid phantoms with both MD-DCS and NIRS. Figure 4(a) shows the measured (fitted by MD-DCS) μ_s' and the agreement with the expected values (slope = 0.9, intercept = 0.4). The absorption coefficient of all phantoms is expected to be the same. As shown in Fig. 4(b), the fitted absorption coefficient of all phantoms (0.0282 ± 0.0007 cm^{-1}) is the same and is in the range of the expected μ_a of water ($\mu_a^{785\,\mathrm{nm}} = 0.02$ to 0.03 cm^{-1}). Since the changes in viscosity due to Lipofundin titration are negligible, it is expected that BFI also does not change by Lipofundin titration. Figure 4(c) shows that the measured BFI ($1.83 \times 10^{-8} \pm 0.06 \times 10^{-8}$ cm^2/s) is constant over all phantoms. We note that the relatively large error bars are due to the protocol that was chosen which, as explained above, involves the lifting and replacement of the probe as it is done for the *in vivo* measurements.

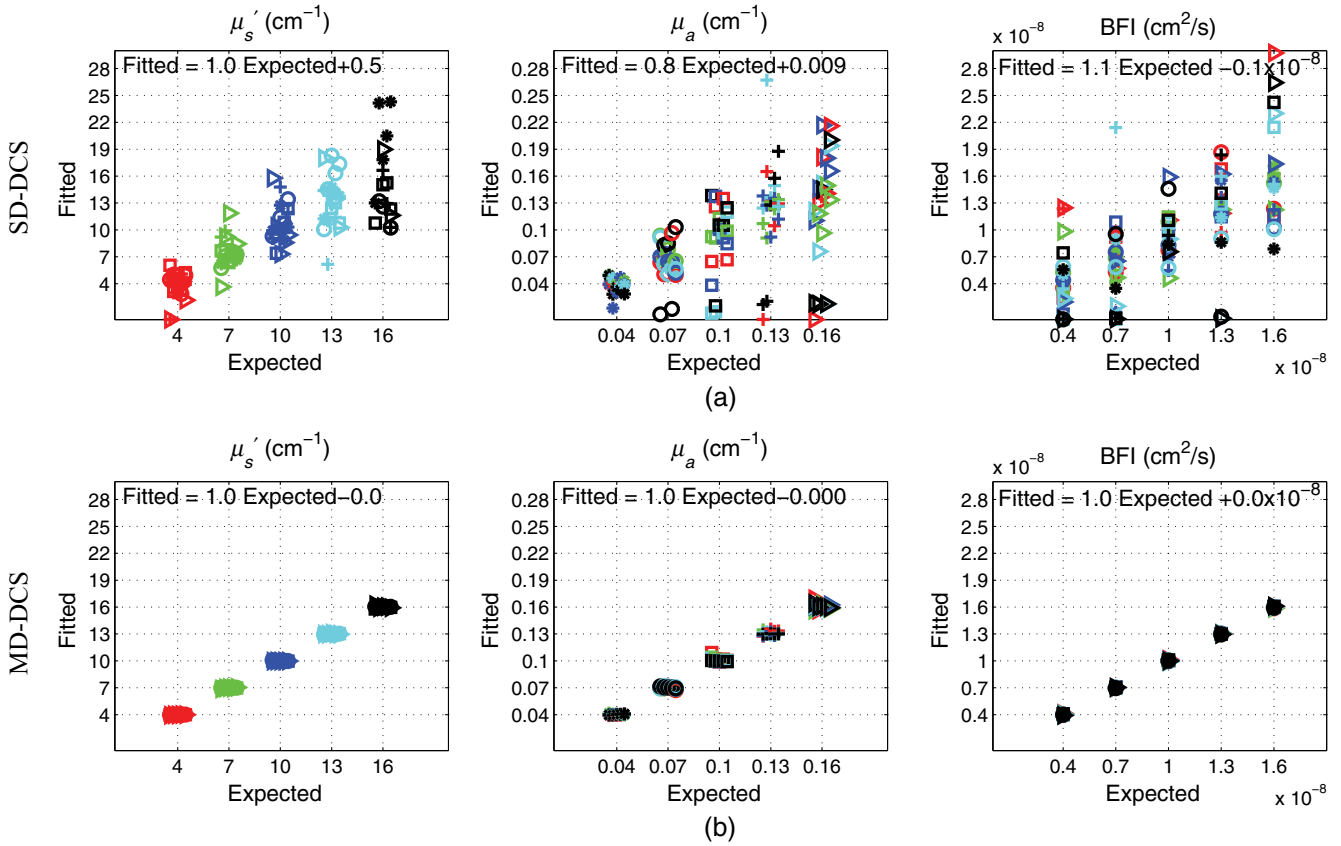

Fig. 3 The values of fitted μ_s', μ_a, and BFI by (a) SD-DCS and (b) MD-DCS versus the expected values in small source-detector separations (2.5 to 5.0 mm). The slope (expected slope is 1) and intercept (expected intercept is 0) of the fitted values versus the expected ones for each parameter are displayed in the inset. (a) SD-DCS has a fairly large error in fitting μ_a, μ_s', and BFI. (b) In MD-DCS, the fitted line for all parameters has a slope of 1 and 0 intercept, which indicate the complete agreement of the fitted and expected values. Each color represents one μ_s' (red: $\mu_s' = 4$, green: $\mu_s' = 7$, blue: $\mu_s' = 10$, cyan: $\mu_s' = 13$, and black: $\mu_s' = 16$) and each μ_a is shown by a different marker (star: $\mu_a = 0.04$, circle: $\mu_a = 0.07$, square: $\mu_a = 0.10$, cross: $\mu_a = 0.13$, and triangle: $\mu_a = 0.16$). Dodging is used (moving the points slightly across the x-axis) for better visualization of BFI values where for each μ_s' or μ_a, BFI increases from left to right.

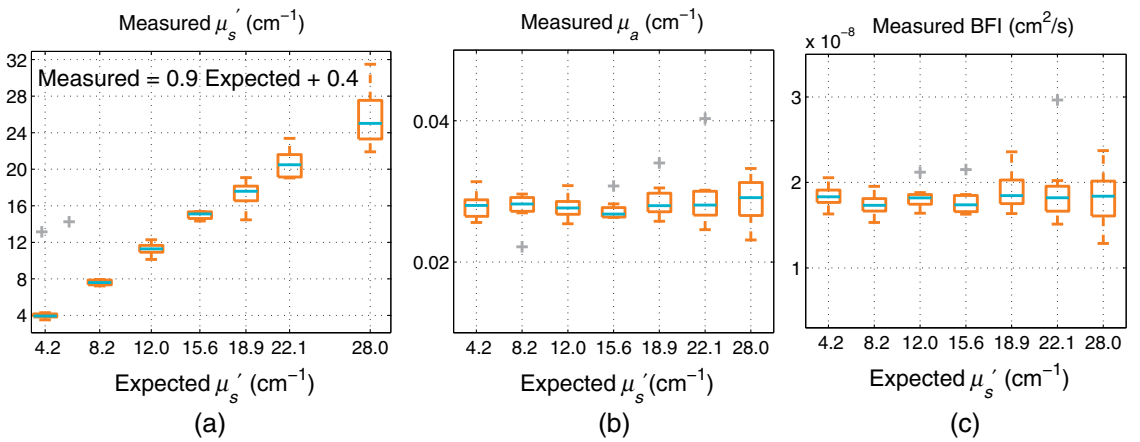

Fig. 4 The measured μ_a, μ_s', and BFI by MD-DCS versus expected values in the liquid phantom measurement. On each box, the central mark is the median and the edges of the box are the 25'th and 75'th percentiles over all 10 relocating measurements. (a) The measured (fitted by MD-DCS) μ_s' versus expected values and their increase in each step of titration. The linear fitting equation of fitted μ_s' versus expected is presented (slope = 0.9, intercept = 0.4). (b) The measured (fitted by MD-DCS) absorption coefficient of all phantoms is the same and in the range of the expected μ_a for water ($\mu_a^{785\,nm} = 0.02$ to 0.03 cm^{-1}). (c) The measured (fitted by MD-DCS fitting) BFI is constant over all phantoms.

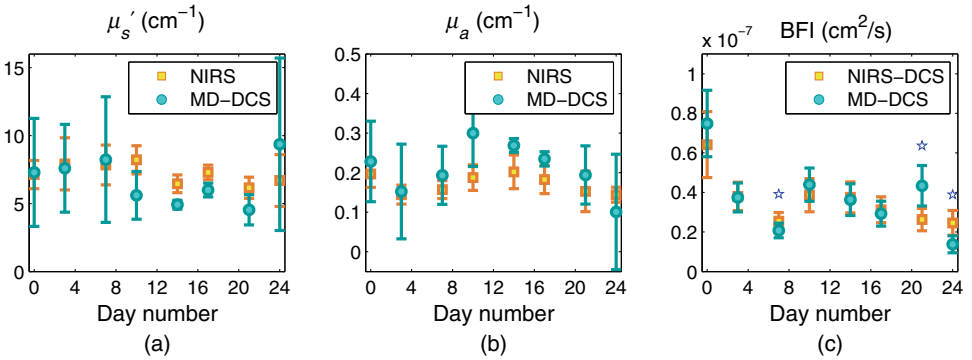

Fig. 5 The fitted values from both methods (MD-DCS and NIRS/DOS) for μ_s', μ_a, and BFI over 24 days on a mouse tumor. The central markers represent the mean values and the error bars show the standard deviation at each day of the measurement. (a) The fitted μ_s' from NIRS/DOS and MD-DCS. (b) The fitted μ_a from NIRS/DOS and MD-DCS. (c) The fitted BFI from hybrid device and standalone MD-DCS. The blue stars show where the null hypothesis of equal means is rejected.

3.4 *Multidistance Diffuse Correlation Spectroscopy Fitting on the Longitudinal In Vivo Data from a Mouse Tumor*

To validate the MD-DCS technique in a more realistic scenario where the heterogeneity of the medium optical properties may pose difficulties to a multidistance measurement, we have applied the method on a mouse tumor. The results of fitting values with both methods (MD-DCS and NIRS/DOS) for all three parameters over 24 days are presented in Fig. 5. Although the fitted μ_a and μ_s' from NIRS/DOS and MD-DCS deviate slightly and MD-DCS has a significantly higher standard deviation, the fitted BFI from both fittings shows a fair agreement.

We have examined the null hypothesis that the BFI values measured by standalone MD-DCS and hybrid device have equal means. The null hypothesis was rejected for only 3 days which are shown by blue stars in Fig. 5.

4 Discussion

In this study, we have introduced an algorithm that utilizes MD-DCS to simultaneously estimate the absolute values of static (reduced scattering and absorption coefficients) and dynamic (blood flow) properties of the tissue. The main goal of this algorithm is to be able to obtain a robust estimate of the BFI even without an independent measurement of the optical properties.

As it was previously shown[7] in traditional DCS fitting (SD-DCS), the cross-talk between optical properties (μ_s' and μ_a) and BFI does not allow the simultaneous fitting of all three parameters. Here, we show that the source-detector separation dependence of g_1 allows us to decouple completely (in case of noise-free data) or partially (under the influence of noise) the contribution of μ_a, μ_s', and BFI by fitting for multiple separations aiming to minimize a single cost function. Figure 1 illustrates this point in an objective manner where it is observed that in the case of the single distance fitting, the minimum of penalty function (χ^2) occurs over a wide range of values which can be translated as the high cross-talk between μ_s' and BFI in SD-DCS. By considering multiple separations, MD-DCS, χ^2 is confined to a smaller area which leads to a better convergence of the algorithm.

To demonstrate that this can be utilized in a fitting algorithm, we have applied SD-DCS and MD-DCS to noise-free data for small, intermediate, and large source-detector separations (Figs. 2, 7, and 8) showing that MD-DCS can accurately retrieve all parameters while SD-DCS has considerable error even in noise-free data and the error increases by increasing the source-detector separation. Since the data are noise-free and the signal-to-noise ratio is not affected by the optode distance, these results demonstrate that, as expected from the cost function, SD-DCS is not a reliable method to simultaneously fit multiple parameters. These results are in agreement with previous work.[7]

Furthermore, SD-DCS has a considerable error when dealing with realistic noise in the simulated data as shown in Figs. 3, 9, and 10. On the other hand, in the noise-added simulated data, we have observed that in the small source-detector regime, MD-DCS fits all parameters with high accuracy (less than 5% error), but by increasing the source-detector separations, the accuracy of the fitted parameters decreases.

We attribute this to the interplay of several factors: for the larger separations the signal-to-noise ratio is worse, the autocorrelation curve decays faster, and the bin size for each delay time is finite. As shown in Eq. (1), the decay of the autocorrelation function depends on the optical properties and BFI via $K(\tau)$ and the source-detector separation ρ. The couplings of the optical properties, in particular μ_s', and BFI are evident in this equation but the strength of the coupling depends on both ρ and the relative values of the τ dependent and independent parts of K. As the signal-to-noise ratio gets worse and the curve decays faster, the sensitivity to different parameters decreases, which becomes even worse by the finite bin size. In the future, a more advanced theoretical analysis may allow for better algorithms to decouple the different parameters.

Our next step was to accept these findings, limit ourselves to smaller source-detector separations, and validate MD-DCS on liquid phantoms with μ_s' titration while μ_a and BFI were kept constant. As was shown in Fig. 4, the measured (fitted by MD-DCS) μ_a, μ_s', and BFI agreed with the expected values. We once more stress that this measurement has validated the algorithm in challenging conditions which resemble the *in vivo* measurements. The liquid phantoms were measured by a handheld probe and for each measurement the probe was removed and then replaced 10 times.

We have then tested the algorithm on our previous measurements[9] from a mouse tumor undergone a longitudinal study after receiving a cancer therapy. In Fig. 5, we have compared the fitted μ_a and μ_s' by NIRS/DOS and MD-DCS, which has demonstrated that the results of MD-DCS alone are noisier than a dedicated NIRS/DOS measurement. This was expected since the NIRS/DOS system used a multidistance, broadband

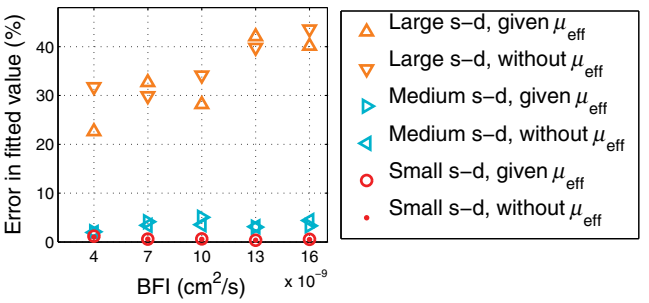

Fig. 6 The error in fitted BFI by MD-DCS on noise-added simulated data for different source-detector separation regimes (small, intermediate, and large). For each source-detector separation range, the estimated error with and without providing μ_{eff} is presented.

dataset with optimized detector sizes for an improved signal-to-noise ratio and a great deal of redundancy. MD-DCS, on the other hand, used small (≈6 μm) single-mode fibers which are not optimized to collect the maximum intensity. However, the BFI results that were shown in Fig. 5 were in good agreement over the majority of the days with a comparable variance. We argue that these results are satisfactory since the goal of this algorithm is to obtain reliable BFI measurements rather than to replace NIRS/DOS.

Finally, we note that for the *in vivo* results we have used estimates of μ_{eff} to constrain the optical properties. We have argued that the continuous-wave DCS laser and the mean intensity could also be used if the source-detector coupling coefficients are calibrated. This illustrates both a possible shortcoming, i.e., the need to constrain the values, and also a potential solution, i.e., the use of the MD-DCS data to estimate that value. To explore this further, in noise-added simulated data, we have tested all the source-detector separation ranges (small, intermediate, and large) and have evaluated the error in fitted BFI (ε_{BFI}) deploying Eq. (4) with and without the knowledge of μ_{eff} as a prior. The estimated error for noise-added data is presented in Fig. 6. It shows that in simulated homogenous media, providing μ_{eff} does not affect the accuracy of MD-DCS considerably when the conditions are near-ideal. However, MD-DCS is highly sensitive to the source-detector separation regime (small, intermediate, and large) and its accuracy dramatically decreases in large optode distances. This means there is more room for further improvement in the experimental implementation of this algorithm.

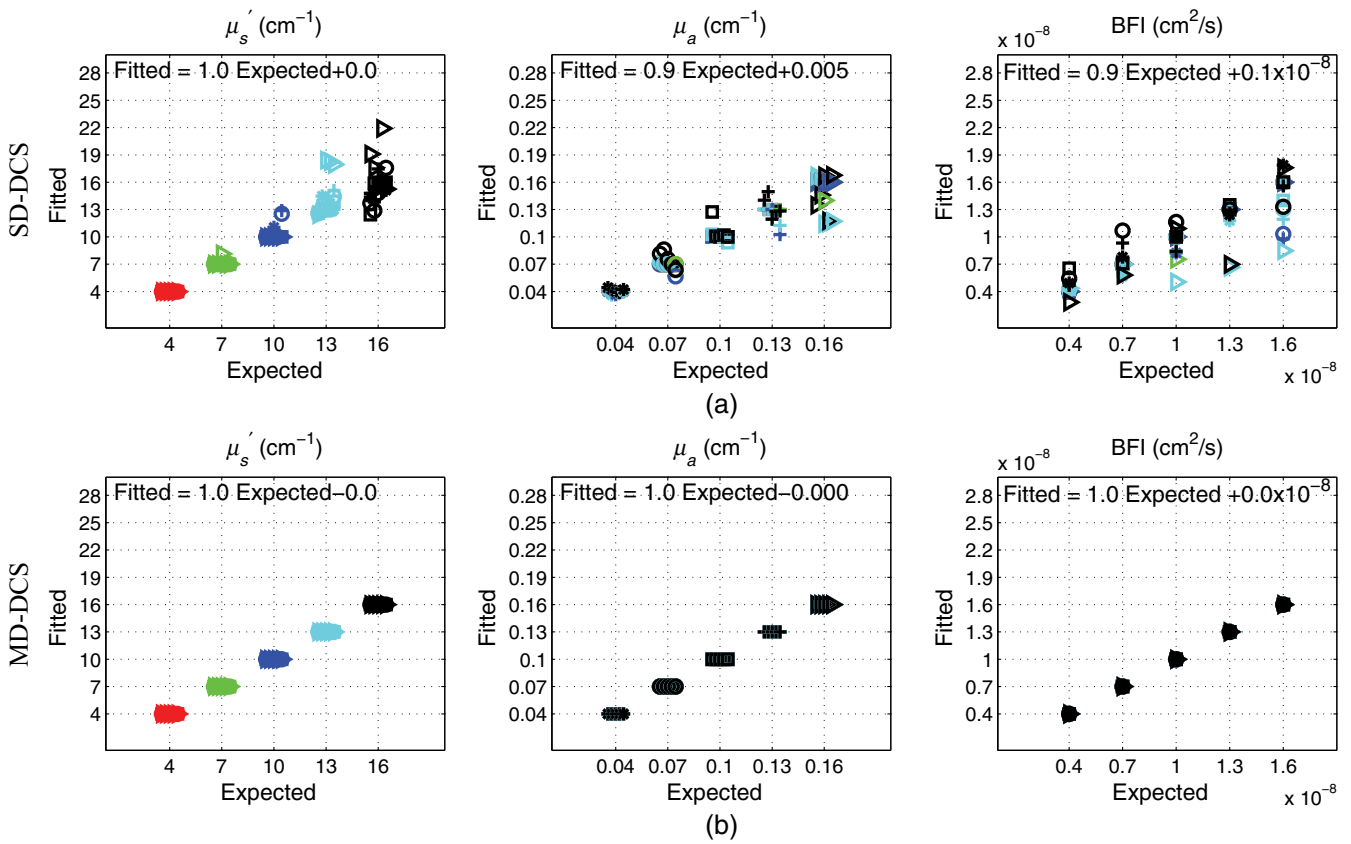

Fig. 7 The values of fitted μ_s', μ_a, and BFI by (a) SD-DCS and (b) MD-DCS versus the expected values in noise-free data of intermediate source-detector separations (10 to 20 mm). The slope (expected slope is 1) and intercept (expected intercept is 0) of the fitted values versus expected ones for each parameter are displayed in the inset. (a) SD-DCS has error in estimation of μ_a, μ_s', and BFI. (b) In MD-DCS, the fitted line for all parameters has slope of 1 and 0 intercept, which indicate the complete agreement of fitted and expected values. Each color represents one μ_s' (red: $\mu_s' = 4$, green: $\mu_s' = 7$, blue: $\mu_s' = 10$, cyan: $\mu_s' = 13$, and black: $\mu_s' = 16$) and each μ_a is shown by a different marker (star: $\mu_a = 0.04$, circle: $\mu_a = 0.07$, square: $\mu_a = 0.10$, cross: $\mu_a = 0.13$, and triangle: $\mu_a = 0.16$). Dodging is used (moving the points slightly across the x-axis) for a better visualization of BFI values where for each μ_s' or μ_a, BFI increases from left to right.

5 Conclusion

We have investigated the possibility of simultaneous extraction of absorption coefficient (μ_a), reduced scattering coefficient (μ_s'), and BFI of the tissue using MD-DCS. Numerical simulations demonstrate that the fitting is more robust in relatively smaller source-detector separations (from 2 to 20 mm). MD-DCS is then validated on tissue simulating phantoms. Finally, it is applied for *in vivo* measurements on a mouse tumor. The results suggest that MD-DCS can be used to decouple the absorption and scattering coefficients from BFI in small source-detector separations to allow simpler, DCS-only approaches in cases where BFI is the primary parameter of interest.

Appendix A: Noise-Free Simulated Data of Intermediate and Large Optode Distances

In this section, the results of SD-DCS and MD-DCS fitting in noise-free data are presented. Figure 7 shows the values of fitted μ_s', μ_a, and BFI fitted by (a) SD-DCS and (b) MD-DCS versus the expected values for intermediate source-detector separations (10 to 20 mm).

In Fig. 8, the results of SD-DCS and MD-DCS on noise-free data in large source-detector separations (20 to 34 mm) are presented. It can be observed that while MD-DCS fits all parameters perfectly without any error, SD-DCS has a considerable error in fitting μ_a, μ_s', and BFI and the error in fitted values rises by increasing the source-detector separations.

Appendix B: Noise-Added Simulated Data of Intermediate and Large Optode Distances

In this section, the results of SD-DCS and MD-DCS fitting in noise-added simulated data are presented. Figure 9 shows the values of fitted μ_s', μ_a, and BFI fitted by (a) SD-DCS and (b) MD-DCS versus the expected values intermediate source-detector separations (10 to 20 mm). It can be observed that while MD-DCS fits all parameters with high accuracy, SD-DCS fails to fit in many cases.

In large source-detector separations (20 to 34 mm) (Fig. 10), the results of SD-DCS and MD-DCS on noise-added data are presented. Similar to intermediate optode distances, SD-DCS fails to fit μ_s', μ_a, and BFI in most points. In MD-DCS, the fitted

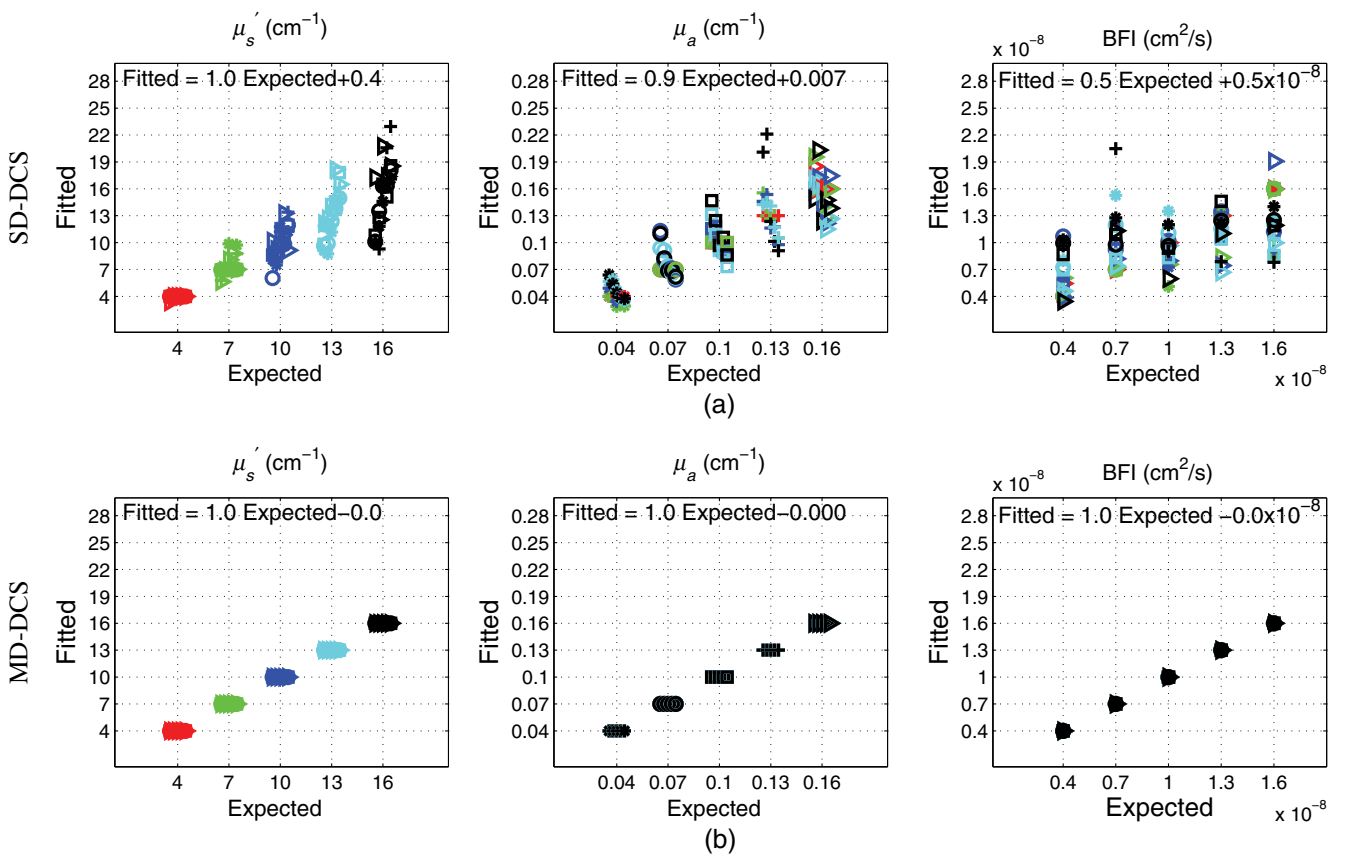

Fig. 8 The values of fitted μ_s', μ_a, and BFI by (a) SD-DCS and (b) MD-DCS versus the expected values in noise-free data in large source-detector separations (20 to 34 mm). The slope (expected slope is 1) and intercept (expected intercept is 0) of the fitted values versus expected ones for each parameter are displayed in the inset. (a) SD-DCS has a considerable error in estimation of μ_a, μ_s', and BFI. (b) In MD-DCS, the fitted line for all parameters has a slope of 1 and 0 intercept, which indicate the complete agreement of fitted and expected values. Each color represents one μ_s' (red: $\mu_s' = 4$, green: $\mu_s' = 7$, blue: $\mu_s' = 10$, cyan: $\mu_s' = 13$, and black: $\mu_s' = 16$) and each μ_a is shown by a different marker (star: $\mu_a = 0.04$, circle: $\mu_a = 0.07$, square: $\mu_a = 0.10$, cross: $\mu_a = 0.13$, and triangle: $\mu_a = 0.16$). Dodging is used (moving the points slightly across the *x*-axis) for better visualization of BFI values where for each μ_s' or μ_a, BFI increases from left to right.

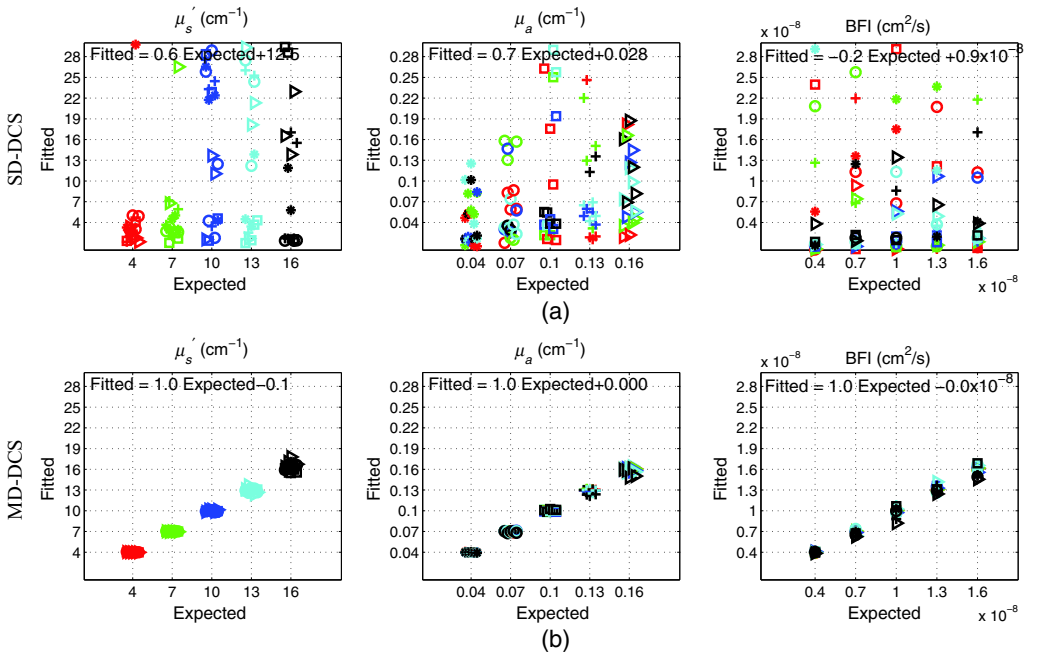

Fig. 9 The values of fitted μ_s', μ_a, and BFI by (a) SD-DCS and (b) MD-DCS versus the expected values in noise-added data of intermediate source-detector separations (10 to 20 mm). The slope (expected slope is 1) and intercept (expected intercept is 0) of the fitted values versus expected ones for each parameter are displayed in the inset. (a) SD-DCS fails to fit μ_a, μ_s', and BFI. Some of the points are not presented since they are out of the *y*-axis range of these plots. (b) In MD-DCS, the fitted values have a good agreement with the expected values. Each color represents one μ_s' (red: $\mu_s' = 4$, green: $\mu_s' = 7$, blue: $\mu_s' = 10$, cyan: $\mu_s' = 13$, and black: $\mu_s' = 16$) and each μ_a is shown by a different marker (star: $\mu_a = 0.04$, circle: $\mu_a = 0.07$, square: $\mu_a = 0.10$, cross: $\mu_a = 0.13$, and triangle: $\mu_a = 0.16$). Dodging is used (moving the points slightly across the *x*-axis) for better visualization of BFI values where for each μ_s' or μ_a, BFI increases from left to right.

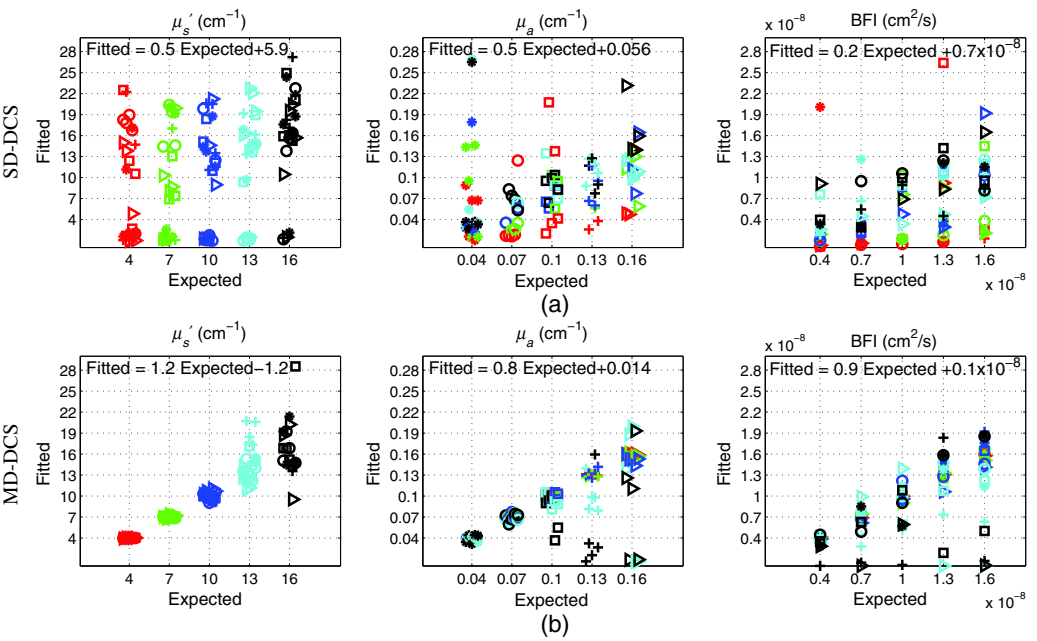

Fig. 10 The values of fitted μ_s', μ_a, and BFI by (a) SD-DCS and (b) MD-DCS versus the expected values in noise-added data in large source-detector separations (20 to 34 mm). The slope (expected slope is 1) and intercept (expected intercept is 0) of the fitted values versus expected ones for each parameter are displayed in the inset. (a) SD-DCS fails to fit μ_s', μ_a, and BFI. Some of the points are not presented since they are out of *y*-axis range of this plots. (b) In MD-DCS, the fitted values have a fair agreement with the expected values in the points where μ_s' and μ_a are small but it fails to fit in high μ_s' and μ_a values. Each color represents one μ_s' (red: $\mu_s' = 4$, green: $\mu_s' = 7$, blue: $\mu_s' = 10$, cyan: $\mu_s' = 13$, and black: $\mu_s' = 16$) and each μ_a is shown by a different marker (star: $\mu_a = 0.04$, circle: $\mu_a = 0.07$, square: $\mu_a = 0.10$, cross: $\mu_a = 0.13$, and triangle: $\mu_a = 0.16$). Dodging is used (moving the points slightly across the *x*-axis) for better visualization of BFI values where for each μ_s' or μ_a, BFI increases from left to right.

values have a fair agreement with the expected values in the points where μ_s' and μ_a are small, but it fails to fit in high μ_s' and μ_a. It can be observed that the accuracy of the fitted parameters by MD-DCS decreases when the source-detector separation is larger than ~2 cm.

Acknowledgments

The project was funded by Fundació Cellex Barcelona, Ministerio de Economía y Competitividad (PHOTOSTROKE), l'Obra Social La Caixa (MedLlumBCN), and LASERLAB Europe III (Bioptichal). We acknowledge useful discussions with Johannes Johansson, Miguel Mireles, and Behrooz Hashemian.

References

1. D. Boas, L. Campbell, and A. Yodh, "Scattering and imaging with diffusing temporal field correlations," *Phys. Rev. Lett.* **75**, 1855–1858 (1995).
2. T. Durduran et al., "Diffuse optics for tissue monitoring and tomography," *Rep. Prog. Phys.* **73**, 076701 (2010).
3. T. Durduran and A. G. Yodh, "Diffuse correlation spectroscopy for non-invasive, micro-vascular cerebral blood flow measurement," *NeuroImage* **85**(Pt 1), 51–63 (2014).
4. E. M. Buckley et al., "Diffuse correlation spectroscopy for measurement of cerebral blood flow: future prospects," *Neurophotonics* **1**, 011009 (2014).
5. G. Yu, "Near-infrared diffuse correlation spectroscopy in cancer diagnosis and therapy monitoring," *J. Biomed. Opt.* **17**, 010901 (2012).
6. D. Irwin et al., "Influences of tissue absorption and scattering on diffuse correlation spectroscopy blood flow measurements," *Biomed. Opt. Express* **2**, 1969–1985 (2011).
7. L. Dong et al., "Simultaneously extracting multiple parameters via fitting one single autocorrelation function curve in diffuse correlation spectroscopy," *IEEE Trans. Biomed. Eng.* **60**, 361–368 (2013).
8. P. Farzam and T. Durduran, "Design of a broadband near infrared spectroscopy (NIRS) and diffuse correlation spectroscopy (DCS) device with a self-calibrated probe for experimental oncology," in *European Conf. Biomedical Optics*, Munich, Germany (2011).
9. P. Farzam, "Hybrid diffuse optics for monitoring of tissue hemodynamics with applications in oncology," PhD thesis, (ICFO-The Institute of Photonic Sciences 2014).
10. C. Zhou et al., "Diffuse optical correlation tomography of cerebral blood flow during cortical spreading depression in rat brain," *Opt. Express* **14**, 1125–1144 (2006).
11. L. Koban et al., "Processing of emotional words measured simultaneously with steady-state visually evoked potentials and near-infrared diffusing-wave spectroscopy," *BMC Neurosci.* **11**, 85 (2010).
12. P. Farzam et al., "Noninvasive characterization of the healthy human manubrium using diffuse optical spectroscopies," *Physiol. Meas.* **35**, 1469–1491 (2014).
13. H.-W. Wang et al., "Broadband reflectance measurements of light penetration, blood oxygenation, hemoglobin concentration, and drug concentration in human intraperitoneal tissues before and after photodynamic therapy," *J. Biomed. Opt.* **10**(1), 014004 (2005).

Parisa Farzam received her PhD in biomedical photonics from ICFO-The Institute of Photonics Sciences, Spain. Her PhD research was focused on developing hybrid diffuse optics for monitoring of tissue hemodynamics with applications in oncology. Currently, she is a postdoctoral researcher at the Institute of Applied Physics at the University of Bern, Switzerland, working on quantitative measurement of preterm-neonate cerebral hemodynamics.

Turgut Durduran was trained at the University of Pennsylvania. In 2009, he moved to ICFO-The Institute of Photonic Sciences, Spain, where he leads the medical optics group. His research interests revolve around the use of diffuse light to noninvasively probe tissue function. The group develops new technologies and algorithms and routinely translates them to preclinical, clinical, and industrial applications.